# Multi-Fidelity Optimization of Hybrid Wing-Body Aircraft with Stability and Control Requirements

Thomas A. Reist[*] and David W. Zingg[†]

*Institute for Aerospace Studies, University of Toronto, Toronto, Ontario, M3H 5T6, Canada*

and

Mark Rakowitz,[‡] Graham Potter,[§] and Sid Banerjee[‡]

*Bombardier Aerospace, Saint-Laurent, Québec, H4S 2A9, Canada*

**Methods of satisfying stability and control (S&C) requirements for hybrid wing-body (HWB) aircraft are investigated using a multi-fidelity multidisciplinary optimization framework. A Reynolds-averaged Navier-Stokes solver is used for aerodynamic prediction, together with conceptual-level weight and balance models. These are coupled with a gradient-based optimizer to form a multidisciplinary optimization tool. Two HWB configurations are investigated. The first uses winglets with winglet-mounted rudders for lateral control, while the second uses centerbody-mounted fins with rudders. Longitudinal control is achieved with one centerbody elevator and six wing-mounted elevons. The designs are optimized for a combination of minimum maximum take-off weight and cruise drag. The ability of the designs to maintain lateral trim with one engine inoperative at a specified minimum control speed and to achieve a given rotational acceleration at a specified rotation speed form the off-design S&C constraints. Additional constraints at cruise ensure trim and a required static margin. In addition to a classical HWB shape, a narrower cabin layout is also considered which provides improved performance. The required S&C requirements are found to be attainable using both configurations, with the fin-based control having a small performance advantage. The narrow centerbody configuration is found to provide superior performance over the classical configuration.**

[*]Research Associate, tom.reist@utoronto.ca

[†]University of Toronto Distinguished Professor of Computational Aerodynamics and Sustainable Aviation, Director, Centre for Research in Sustainable Aviation, and Associate Fellow AIAA, dwz@oddjob.utias.utoronto.ca

[‡]Senior Engineering Specialist, Advanced Design, Product Development Engineering

[§]Engineering Specialist, Advanced Design, Product Development Engineering

# Nomenclature

**Symbols**

| | |
|---|---|
| $\mathit{Æ}$ | Aspect ratio ($\mathit{Æ} = b^2/S$) |
| $\mathit{Æ}_{\text{wet}}$ | Wetted aspect ratio ($\mathit{Æ}_{\text{wet}} = b^2/S_{\text{wet}}$) |
| $\alpha$ | Aircraft angle-of-attack [°] |
| $b$ | Total span [ft] |
| $\beta$ | Aircraft side-slip angle [°] |
| $c$ | Local chord length [ft] |
| $c_l, c_d, c_m$ | Section lift, drag, and pitching moment coefficients, respectively |
| $C_L, C_D, C_Y$ | Aircraft lift, drag, and side-force coefficients, respectively |
| $C_l, C_m, C_n$ | Aircraft roll, pitch, and yawing moment coefficients, respectively |
| $\delta_e, \delta_r$ | Elevon/elevator and rudder deflections, respectively [°] |
| $\Delta$ | Change in variable |
| $\Delta NP_{\delta/\alpha}$ | Change in neutral point location due to change in control surface deflection or AoA |
| $\Gamma$ | Dihedral [°] |
| $I_{y,o}$ | Mass moment of inertia about axis pitch axis w.r.t. reference point $o$ [$\text{slug} - \text{ft}^2$] |
| $\lambda$ | Taper ratio |
| $\Lambda_n$ | Sweep of the $n^{\text{th}}$ chord line [°] |
| $L, D, Y$ | Lift, drag, side-force [lb] |
| $l_o, m_o, n_o$ | Aircraft roll, pitch, and yawing moment, respectively, about point $o$ [lb-ft] |
| $L/D$ | Lift-to-drag ratio |
| $K_{n_o}$ | Static margin w.r.t. reference point $o$ [% MAC] |
| $S$ | Reference wing area [$\text{ft}^2$] |
| $S_{\text{wet}}$ | Wetted area [$\text{ft}^2$] |
| $\theta$ | Local twist angle [°] |
| $t$ | Section thickness [ft] |
| $t/c$ | Section thickness normalized with local chord length |
| $T$ | Thrust [lb] |
| $V$ | Speed, volume [kts, $\text{ft}^3$] |
| $V_{\text{MC}_\text{G}}$ | Minimum control speed, on ground [kts] |
| $V_R$ | Rotation speed [kts] |
| $W$ | Aircraft weight [lb] |
| $\ddot{\theta}$ | Pitch acceleration [°/$\text{sec}^2$] |

American Institute of Aeronautics and Astronautics

| $x$, $y$, $z$ | Streamwise, spanwise, and vertical coordinates, respectively  [ft] |

**Abbreviations**

| AoA | Angle-of-attack |
| HWB | Hybrid wing-body |
| CFD | Computational fluid dynamics |
| CG | Center of gravity |
| CS | Control surface |
| FFD | Free-form deformation |
| MAC | Mean aerodynamic chord |
| MFW | Maximum fuel weight |
| MLG CP | Main landing gear contact point |
| MTOW | Maximum take-off weight |
| MZFW | Maximum zero-fuel weight |
| NP | Neutral point |
| OEW | Operating empty weight |
| OML | Outer mold line |
| S&C | Stability and control |
| SLS | Sea level static |
| w.r.t. | With respect to |

**Subscripts**

| 0 | Initial value, fixed value, reference value |
| $\infty$ | Freestream value |
| CG | W.r.t.  center of gravity |
| $c/4$ | Quarter chord |
| MLG CP | W.r.t.  main landing gear contact point |
| r | Root |
| ref | Reference value |

# I. Introduction

Hybrid wing-body (HWB) aircraft have been studied extensively over the past several decades due to their potential to be more efficient than conventional designs. However, one of the challenging aspects of their design is the lack of an empennage, which makes satisfaction of stability and control (S&C) requirements more challenging. As part of the X-48 program, wind tunnel and free flight tests were performed to investigate the S&C behaviour of an HWB configuration.[1] The HWB studied had both winglet-mounted rudders and outboard split elevons which could serve as drag rudders. Lateral control authority at low speed was found to be particularly challenging with this configuration. Rahman and Whidborne[2] compared the lateral control authority of both winglet and fin-equipped HWBs, and found that, for the configuration studied, the winglet-mounted rudders were insufficient to maintain lateral trim with asymmetric thrust. The same authors also studied the use of blown control surfaces for longitudinal control.[3] Cook and de Castro[4] studied both static and dynamic stability and control of a large HWB, and demonstrated the limited static margin range in which longitudinal trim can be attained at low speed. Garmendia et al.[5] compared a number of trailing-edge control surface layouts, using between 7 and 11 control surfaces in different configurations, with the aim of minimizing weight, power, and fuel burn. The same authors also studied the control power implications of various control configurations, stability requirements, and turbulence levels.[6]

All of the works discussed above used a fixed planform and studied the control effectiveness of the set configuration. In most cases, aerodynamic and control behaviour was based on linear aerodynamic models. Mader and Martins[7] incorporated both static and dynamic longitudinal stability constraints into an aerodynamic shape optimization framework and applied this to the optimization of a pure flying wing with a free planform, where the longitudinal stability requirements formed constraints.

The present work includes S&C requirements in the multidisciplinary optimization (MDO) of HWB aircraft where the configuration planform is variable, such that the impact of S&C requirements on the system-optimal design can be determined. To that end, a multi-fidelity multidisciplinary framework has been developed which uses low-fidelity weight and balance models and a Navier-Stokes solver for determination of aerodynamic performance, stability derivatives, and control effectiveness. These are coupled with a gradient-based optimizer.

The objectives of this paper are to use this MDO framework to 1) establish the controllability of regional-class HWBs using both winglet-based and fin-based lateral control surfaces, and to compare the performance of these two control configurations, and 2) investigate an alternative HWB layout with a narrower and more elongated centerbody, which has been shown in past work to be more efficient for smaller aircraft.[8] Both longitudinal and lateral S&C requirements are considered. The paper is structured as follows: Section II describes the optimization framework used, Section III presents the details of the design problem under

consideration and its formulation as an optimization problem, including the S&C requirements considered, Section IV presents the optimization of both winglet and fin-equipped HWBs and compares the merits of these two control methods, Section V presents the narrower HWB layout, which proves to be more efficient than the classical HWB configuration, and Section VI examines additional control criteria and the impact of various S&C requirements on performance.

## II.   Optimization Framework

The optimization methodology used is based upon an aerodynamic shape optimization methodology that consists of three main components: 1) a multiblock Newton-Krylov-Schur solver for the Reynolds-averaged Navier-Stokes (RANS) equations with the one-equation Spalart-Allmaras turbulence model,[10] 2) a B-spline geometry parameterization which is coupled with an integrated linear elasticity mesh movement strategy,[11] and 3) the gradient-based optimizer SNOPT[12] with gradients calculated using the discrete adjoint method.[11, 13]

The flow solver is a parallel implicit solver that uses summation-by-parts operators for spatial discretization and simultaneous approximation terms for the imposition of boundary conditions and block interface conditions. The Krylov subspace method Generalized Minimum Residual (GMRES) is used with approximate Schur preconditioning in an inexact Newton method for the solution of the discrete equations. Details of the flow solver can be found in Hicken and Zingg[9] and Osusky and Zingg.[10] The flow solver has been validated through participation in the 5th AIAA Drag Prediction Workshop.[14]

At each optimization iteration for which a geometric shape change occurs, the computational grid must be moved to reflect this change. To accomplish this, each block of the computational grid is fitted with a B-spline volume. The B-spline parameterization on the surface is embedded within a free-form deformation volume that can be controlled through 'axial curves', as described by Gagnon and Zingg[15]. As the B-spline control points on the aerodynamic surface are moved, each B-spline volume block is treated as a linear elastic solid, for which a finite-element solution is obtained to define the new shape of the B-spline volume. The computational grid is then recovered from this new B-spline volume. This method has been found to be very robust for large shape changes while being relatively inexpensive. Details can be found in Hicken and Zingg[11].

Due to the high cost of evaluating the flow equations, a gradient-based optimizer is used for optimization, as gradient-based optimizers typically require fewer function evaluations than genetic algorithms[16]. The gradients of the objective and constraints are evaluated using the discrete adjoint method. The number of adjoint solutions required is proportional to the number of objectives and constraints which depend on the flow properties. Since this can require significant computational cost for practical problems, an efficient
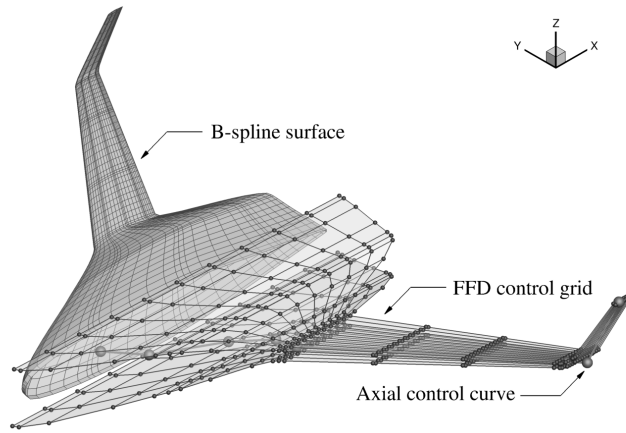
American Institute of Aeronautics and Astronautics

**Figure 1: The geometry control system, including the B-spline surfaces, FFD volumes, and axial control curves.**

method of solving the linear system of the adjoint problem is required. For this, a modified, flexible version of the Generalized Conjugate Residual with Orthogonalization and Truncation (GCROT) algorithm is used[17]. The gradient-based optimizer SNOPT is used, as it allows for the solution of large-scale constrained problems. Details of the adjoint method and its integration with the flow solver and mesh movement are given by Hicken and Zingg[11], while the details of SNOPT are described by Gill et al.[12]

In this work, this methodology has been augmented with low-fidelity structural, balance, and propulsion models and aerodynamic corrections to allow it to serve as a multi-fidelity MDO code. The details of these additions are described below.

## A.   Geometric Control

A free-form deformation (FFD)-based geometry control system is used in this work.[15] To make changes to the planform, the optimizer has control of axial curves which drive the location of FFD control volumes, which in turn can be manipulated to control taper, twist, and section shape. A B-spline parameterization of the aircraft surface is embedded in these FFD control volumes, such that changes to the axial curves and FFD volumes are propagated to the surface parameterization. These components are illustrated in Figure 1.

As part of this work, a method of modelling control surface deflections is required. Such a system was integrated with the geometry control framework described above. To model trailing-edge surface deflections, the FFD control points over the aft portion of the airfoil, the number of which is determined by the desired chord of the control surface, are rotated about a specified hinge line. This rotation then deflects the geometry trailing edge, as illustrated in Figure 2. Figures 2(a) and 2(b) show the undeflected and deflected FFD volumes, respectively, and Figure 2(c) and 2(d) show the resulting surfaces. This control surface model maintains a continuous outer mold line (OML), which maintains the degree of continuity of the underlying geometry, i.e. control deflections do not introduce gaps or slope/curvature discontinuities.
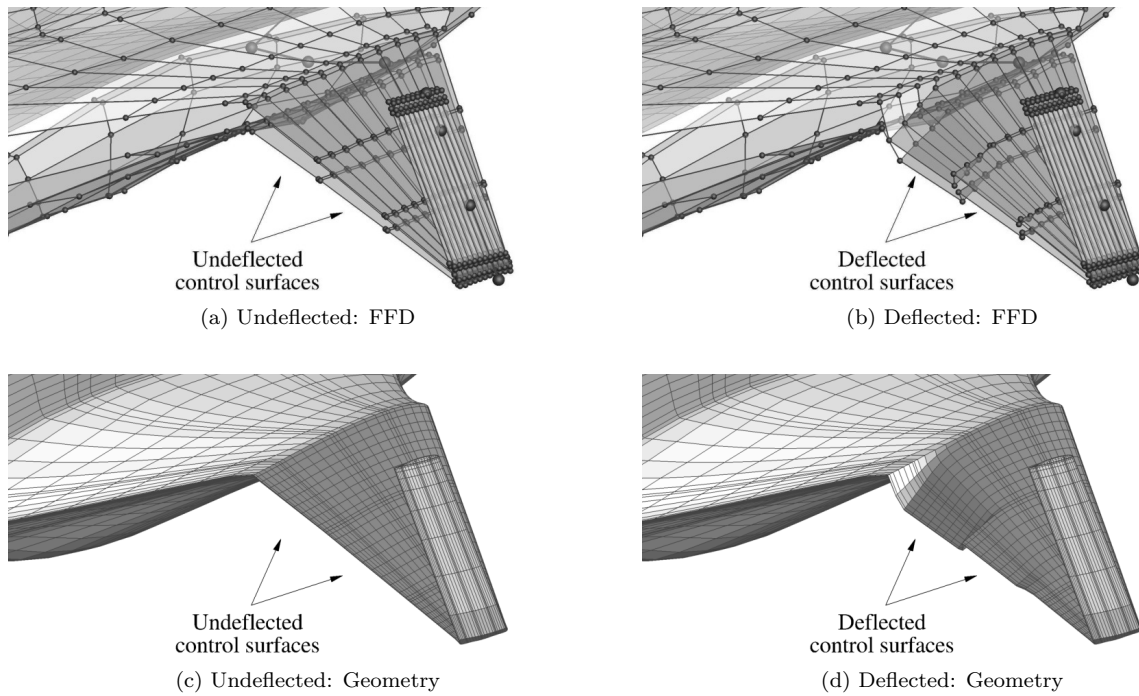
(a) Undeflected: FFD



(b) Deflected: FFD



(c) Undeflected: Geometry



(d) Deflected: Geometry

**Figure 2: Surface deflections caused by rotations of the trailing edge portion of the FFD control grid.**

Since this is a simplified control surface model due to the fact that the section deflects in a continuous manner without any break in slope or curvature at the hinge, validation of its suitability for accurately representing a real control surface is required. Due to a lack of publicly available 3D models and data, experimental data for a two-dimensional NACA 66(215)-216 section with a 20% sealed plain flap is used.[18] The experiments were conducted at a Reynolds number of $6.0 \times 10^6$, and the results are corrected for tunnel effects.

Since the control surface model is only implemented in 3D, an unswept rectangular wing with $Æ = 10$ was used in the computations, and aerodynamic data was only obtained over 20% of the inboard wing so as to help eliminate 3D effects and thus mimic a 2D section. Computations were performed on a $2.2 \times 10^6$ node grid with an average off-wall spacing of $y^+ \approx 1.0$. Deflections of $\delta = 0°, 10°, 20°, 30°$ (the range of deflections seen in the optimizations) were tested for a range of AoA, the results of which are shown in Figure 3 together with the experimental data. The solid circles in the figure indicate values obtained through Richardson extrapolation for $\delta = 10°$ on a family of grids with up to $8.5 \times 10^6$ nodes.

Agreement in $c_l$ and $c_m$ between the experimental and CFD results is good up to before stall, which is predicted early. Increased grid refinement, indicated by the solid circles, leads to better prediction near stall. Drag is not considered here, as the experimental data is 2D, while the CFD results are with a high aspect ratio 3D wing. The experimental data is not smooth near 0° angle of attack (AoA). In fact, in the experimental source documentation, there are multiple results near 0° AoA. The CFD results are smooth

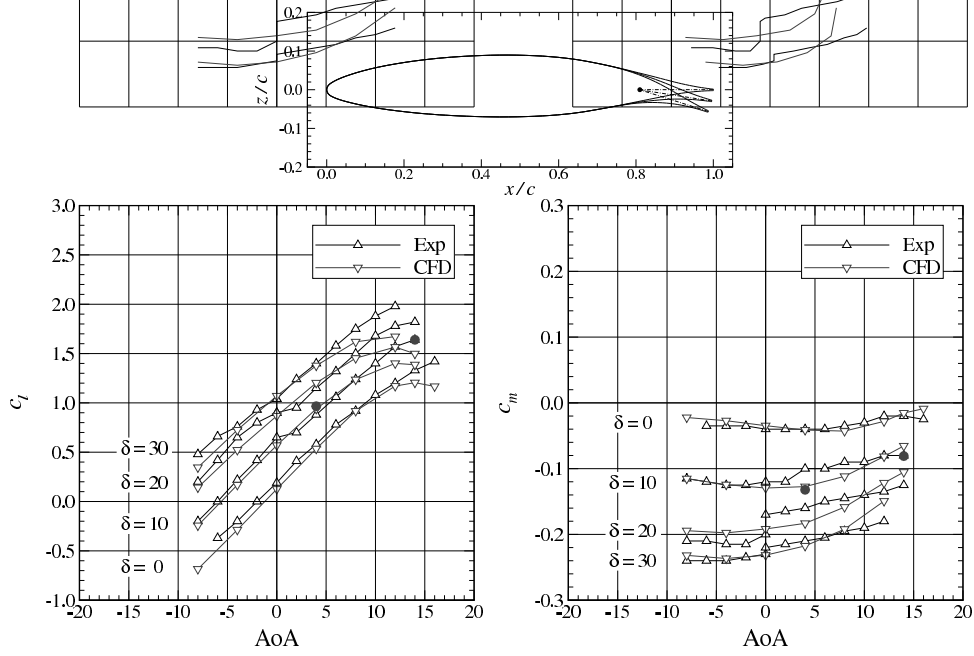American Institute of Aeronautics and Astronautics

Figure 3: Comparison of experimental and CFD data for the NACA 66(215)-216 with a 20% chord sealed plain flap. The solid circles indicate estimates of grid-converged values with $\delta = 10°$.

across the range of AoA, and fall between the experimental results near 0° AoA. Based on the above results, for the purposes of this work, the FFD-based control surface model is deemed to be sufficiently accurate in capturing the aerodynamic forces and moments, and thus suitable for optimization.

## B. Aerodynamic Models

The RANS solver provides the sum of the parasitic and induced drag of the main airframe. Multiblock structured grids which follow the local resolution guidelines of the AIAA Drag Prediction Workshop[19] are used in this work. The same method as described in Reist and Zingg[8] is used to size the grids to ensure trade-offs are captured correctly due to different drag sources and to determine grid-converged estimates. The winglet-equipped HWBs use $2.4 \times 10^6$ node grids and the fin-equipped HWBs use $3.8 \times 10^6$ node grids. All grids have average off-wall spacings of $y^+ \approx 1$. The off-design conditions, as will be detailed later, are analyzed in ground effect. A moving ground plane is used, with a flow tangency boundary condition and a prescribed velocity equal to the airspeed imposed on the ground plane.

Since drag is overpredicted on coarse grids, correction factors are calculated between the optimization level grid and the grid-converged value. These are applied to the drag during the optimization in order to account for grid resolution deficiencies and hence to properly size the fuel loads. Similar correction factors are calculated and applied for the other forces and moments, but their magnitude is significantly smaller than for drag. Unique correction factors are applied to the forces and moments at each operating point. All of the results presented in this paper are computed on the optimization-level grids with the correction

American Institute of Aeronautics and Astronautics

factors applied to estimate the grid-converged values.

Since only the main airframe is modelled with RANS, additional drag models are require to account for drag sources which are not included in the high-fidelity model, such as excrescence drag, nacelle drag, and windmilling drag. These are outlined below.

*1.  Excrescence Drag*

For conceptual design, both Torenbeek[20] and Raymer[21] suggest excrescence drag can be approximated as a constant factor of parasitic drag. As per Raymer, a 5% mark-up is applied to the parasitic drag, as

$$C_{D_{\text{excr}}} = 0.05 C_{D_0} \tag{1}$$

where the parasitic drag, $C_{D_0}$, is given by,

$$C_{D_0} = F C_F \frac{S_{\text{wet}}}{S} \tag{2}$$

where $F$ is a form factor, and $C_F$ is the skin friction coefficient, which is approximated using the Mach number corrected Prandtl-Schlichting relation for turbulent flow,

$$C_F = \frac{0.455}{(\log Re)^{2.58}(1 + 0.144M^2)^{0.65}} \tag{3}$$

Equation 3 is used to obtain $C_F$ instead of the RANS solution, as using the RANS solution would require an additional adjoint solution, thus increasing cost, which is not warranted due to the approximate nature of the excrescence markup. RANS analysis has found the Prandtl-Schlichting relation to be accurate for the flows considered in this work, with a form factor of $F = 1.20$ being appropriate.

*2.  Nacelle Drag*

To reduce cost, the nacelles are not included in the full 3D CFD model, and instead their parasitic drag contribution is accounted for via Equation 2, with $F = 1 + 0.35 d_{\text{nac}}/l_{\text{eng}}$, where $d_{\text{nac}}$ is the nacelle diameter, and $l_{\text{eng}}$ is the nacelle length.[21] The wetted area, $S_{\text{wet}}$, and Reynolds number used for $C_F$ are those of the nacelle. This only accounts for the parasitic contribution of the nacelle drag. For HWB aircraft, special consideration of the interactions of the centerbody upper surface and nacelle/pylon must be accounted for to reduce interference drag. This interference drag is not accounted for in this work.

American Institute of Aeronautics and Astronautics

### 3. Windmilling Drag

The windmilling drag of an inoperative engine is captured via the relation

$$C_{D_{\text{wm}}} = \frac{3\pi d_{\text{fan}}^2}{40S} \qquad (4)$$

given by Raymer,[21] where $d_{\text{fan}}$ is the fan diameter. This accounts for both internal and external drag of the inoperative engine.

### C. Weight Models

The structural, fixed, and fuel weights are calculated using the relations detailed in the following subsections, and feed into the following equations, which are solved in an iterative manner:

$$\text{OEW} = W_{\text{centerbody}} + W_{\text{wing}} + W_{\text{winglets/fins}} + W_{\text{engines}} + W_{\text{fixed}} \qquad (5)$$

$$\text{MTOW} = \text{OEW} + W_{\text{design payload}} + W_{\text{design fuel}} \qquad (6)$$

where the design payload and fuel correspond to the design mission.

### 1. Centerbody Weight

The centerbody weight model developed by Bradley[22] is used, which is a function of MTOW, pressurized cabin area, unpressurized area aft of the cabin, and the taper ratio of the aft area. The results of this model have been compared against higher fidelity analysis for small HWB aircraft and have been found to be in good agreement. This model assumes the use of carbon fiber reinforced composites for the pressure vessel, but not advanced structural solutions such as PRSEUS.[23] Thus, weight reduction may be possible if such advanced structural concepts are used.

### 2. Wing Weight

The wing (that portion of the wing outboard of the passenger cabin) is treated as a conventional cantilever wing, for which the wing weight model of Torenbeek is used.[20] This model is for simple trapezoidal wings, so the more complicated multi-segment HWB wings are transformed into a trapezoidal wing to which the model can be applied. The transition region and main wing are combined into a trapezoidal wing of area and span equivalent to the sum of the transition and main wing. The sweep angle of the trapezoidal wing is the span-weighted average of the two segment sweep angles. The resulting equivalent wing is shown in Figure 4. In addition, since the centerbody carries a significant portion of lift, the loading term, MZFW, is scaled by the fraction of lift that the wing carries.
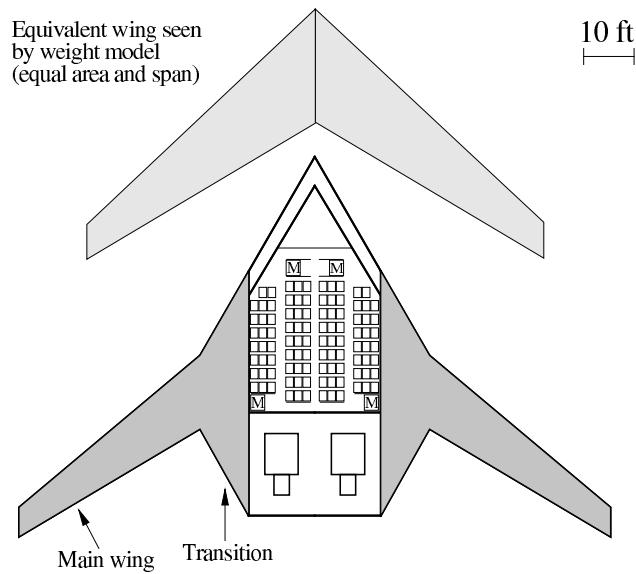
**Figure 4: Sample HWB with the true and equivalent wings seen by the weight model.**

*3. Winglet/Fin Weight*

The weight model for the winglets and body-mounted fins is based on Bombardier internal data and is a function of the winglet/fin wetted area.

*4. Engine Weight*

Engine weight, dimensions, sea level static (SLS) thrust, and thrust specific fuel consumption are obtained by scaling of Bombardier internal reference engine data. The reference values are scaled as a function of $T/T_{\text{ref}}$, where $T$ is the thrust required to achieve a rate of climb of $300\,\text{ft/min}$ at the top of climb for the design mission, and $T_{\text{ref}}$ is the thrust available at cruise for the reference engine.

*5. Fuel Weight*

Cruise fuel is calculated via the Breguet range equation, while additional stages of flight are accounted for through fuel fractions. A single stage cruise-climb cruise profile is assumed, with the lift-to-drag ratio being that at the start of cruise for the design mission (as will be described in Section III). Reserve fuel for a $100\,\text{nmi}$ diversion and $45\,\text{min}$ hold is also included.

*6. Fixed Weights*

Other weights, including landing gear, hydraulics, operational items, etc. are assumed to be only weakly dependent on design changes made by the optimizer and are thus treated as a constant. A low-fidelity conceptual design sizing code based on the relations of Torenbeek,[20] Roskam,[24] and Raymer[21] is used to

American Institute of Aeronautics and Astronautics

size the above fixed weights.[25]  For a regional-class aircraft the above fixed weights are computed to be $W_{\text{fixed}} = 24,000\,\text{lb}$.

### 7. Center of Gravity Estimation

Both the center of gravity (CG) positions and the longitudinal moment of inertia are required for balance and rotation analysis.  The following assumptions are made in the calculation of the CG of the various components:

Centerbody: The centerbody structural weight acts at the volume centroid of the centerbody OML.

Wing: The wing structural weight acts at the volume centroid of the wing OML.

Winglet/Fin: The winglet and fin structural weight acts at the volume centroid of the winglet/fin OML.

Engines: The engine is positioned such that the thrust line is laterally offset by one nacelle diameter from the aircraft centerline, and vertically offset by one and a half nacelle diameters above the chordline at the aircraft centerline, and the exhaust exit is one nacelle diameter upstream of the centerbody trailing edge. The engine weight acts along the thrust line, and at the engine mid-point.

Fuel: The fuel weight acts at the volume centroid of the wing OML. Fuel is only stored in the outboard wing, and not in the centerbody/wing transition region.

Payload: The payload weight acts at the centroid of the cabin.

Fixed: The fixed weights are assumed to act at the same location as the centerbody CG.

The pitch moment of inertia is calculated by taking the integral of the 2$^{\text{nd}}$ moment of mass over the OMLs of the above components, where the mass of each component is assumed to be distributed evenly within that component.

### 8. Main Landing Gear Positioning

The main landing gear (MLG) position comes into play in several of the geometric and S&C constraints. The MLG is positioned 10° aft of the aft-most CG location. The lateral position of the MLG is assumed to be 2 ft outboard of the cabin. While no constraint explicitly ensures sufficient stowage space, the resulting designs have unused space outboard of the cabin as a result of the decreasing thickness of the transition region, in which it is assumed stowage space can be made without changing the conclusions of this study. The location of the nose gear does not impact any of the S&C criteria included in this work, and is thus not considered.
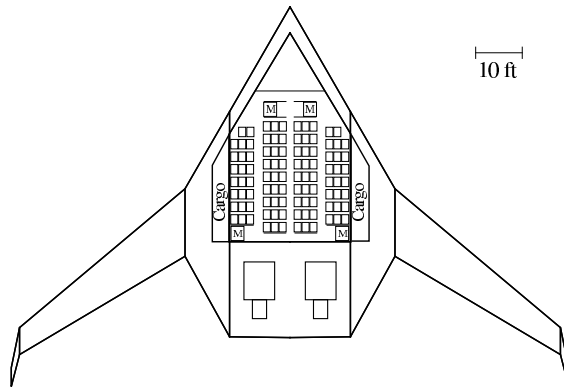
**Figure 5: Layout of the initial HWB. Winglet-equipped configuration shown. Seats, monuments (galleys, lavatories), and cargo compartments are identified.**
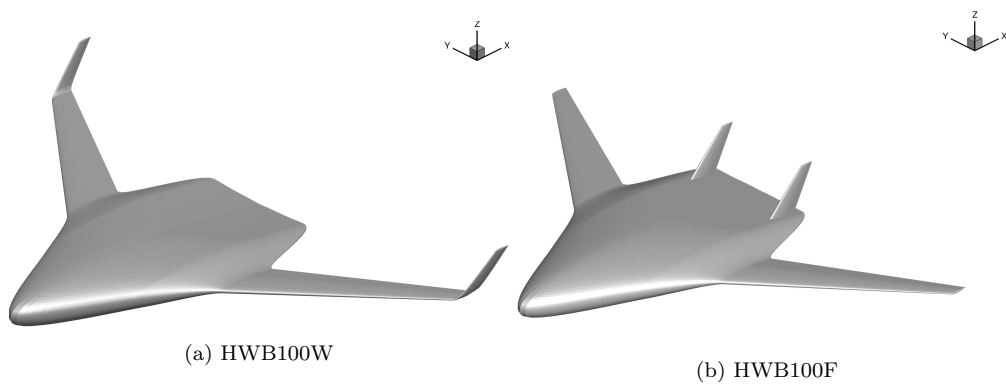


(a) HWB100W

(b) HWB100F

**Figure 6: Initial HWB models.**

## III.  Design Problem

This work is based upon a 100-passenger regional-class HWB with a range of 2,000 nmi at full passenger payload (22,500 lb). The designs will be optimized for a combined weight/drag objective, as described below, and will be subject to both longitudinal and lateral S&C requirements. The details of the optimization problem, including the S&C constraints, are given below.

The initial concepts, which are similar to those presented by Reist and Zingg,[8] form the starting point for the creation of full three-dimensional models. The layout of the winglet-equipped HWB is shown in Figure 5. The layout of the fin-equipped HWB is the same, with the winglets replaced with fins.

The three-dimensional models based upon these layouts are shown in Figure 6 for both configurations. In this paper, HWB100W will refer to winglet-equipped designs, while HWB100F will refer to fin-equipped deigns. Initially, the designs use symmetric sections with zero spanwise twist; these will be designed by the optimizer. The centerbodies use 14% thick SC(2)-0012 sections, with SC(2)-0012 and SC(2)-0010 sections at the wing root and tip, respectively. The fin-equipped HWB uses SC(2)-0010 sections for the vertical fins.

Aircraft views are shown with $x$ in the streamwise direction, $y$ out the right wing, and $z$ upwards, with

American Institute of Aeronautics and Astronautics

**Table 1: Optimization problem formulation. See Figure 7 for an illustration of the geometric design variables.**

| | | |
|---|---|---|
| **Objective** | | minimize $\frac{1}{2}\frac{\text{MTOW}}{\text{MTOW}_{\text{ref}}} + \frac{1}{2}\frac{D}{D_{\text{ref}}}$ |
| **Design variables** | Geometric: | See Table 2 |
| | Cruise: | $-2.5° \leq \text{AoA} \leq +2.5°$ |
| | $V_{\text{MC}_{\text{G}}}$-proxy: | $0.0° \leq \text{AoA} \leq +2.0°$ |
| | | $-30° \leq \delta_r \leq +30°$ ($\times 2$) |
| | Rotation: | $0.0° \leq \text{AoA} \leq +2.0°$ |
| | | $-25°/3 \leq \delta_e \leq +25°/3$ ($\times 7$) |
| **Constraints** | Geometric: | See Table 2 |
| | | Cabin shape constraint |
| | | Wing fuel volume |
| | | Tip strike clearance |
| | | Ground clearance |
| | Cruise: | $L = W$ |
| | | $\Sigma m_{\text{CG}} = 0$ |
| | | $K_{n_{\text{CG aft}}} \geq -4\%$ |
| | $V_{\text{MC}_{\text{G}}}$-proxy: | $\Sigma n_{\text{MLG CP}} = 0$ |
| | Rotation: | $L \geq 0$ |
| | | $\Sigma m_{\text{MLG CP}} \geq I_{y,\text{MLG CP}}\ddot{\theta}$ |

the origin at the aircraft nose. Moments are given relative to the body-fixed axes, where $x$ points forward, $y$ out the right wing, and $z$ downwards. Pitching moments are nondimensionalized by the reference mean aerodynamic chord (MAC), while yaw and rolling moments are nondimensionalized by the total span.

## A. Optimization Problem Formulation

This section describes the optimization problem formulation, including objective function, design variables, and constraints. The objective is minimized at the cruise design point, and is subject to both on and off-design constraints. The off-design constraints are imposed at two conditions; a minimum control speed on ground ($V_{\text{MC}_{\text{G}}}$) proxy case to ensure sufficient lateral control, and a rotation case to ensure sufficient rotation authority. The problem is summarized in Table 1, with details given below.

### 1. Objective and Operating Points

The objective to be minimized is a normalized composite of 50% MTOW and 50% drag at the design point. This makes the objective of order unity. Choosing an appropriate objective is challenging, and can have a significant impact on the optimization problem. The inclusion of MTOW in the objective captures many aspects of aircraft performance, including manufacturing costs, fuel burn, and operating expenses, to name a few, and is a common objective in aircraft design. The addition of a drag term puts additional emphasis on fuel burn. This 50/50 combination has been found to be a good design metric, which places additional
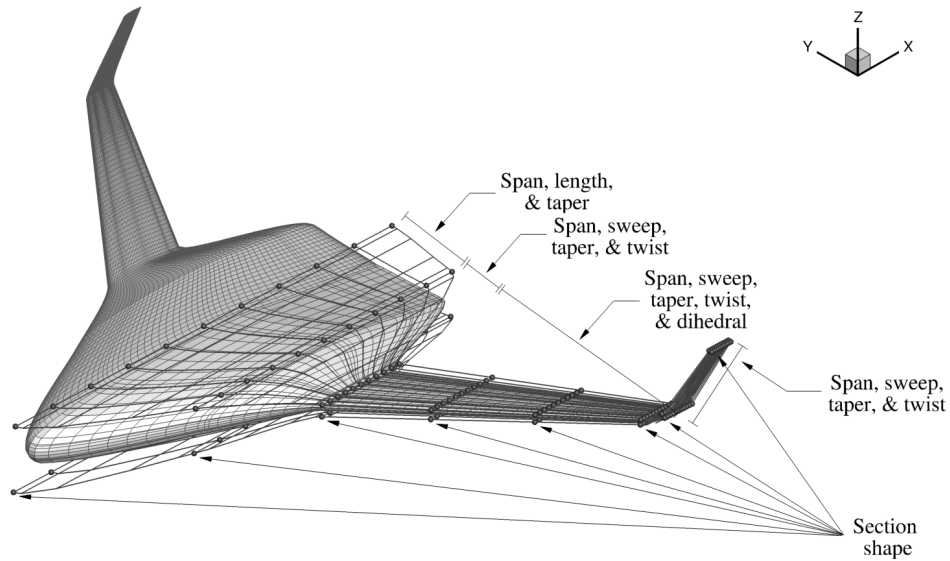
**Figure 7: Geometric design variables.**

emphasis on environmental performance.

Three operating points are considered in the optimization:

1. Cruise: The cruise point is analyzed at the start of the 2,000 nmi mission with full payload. Cruise at Mach 0.78 and 36,000 ft is assumed. This point is used as the analysis point for the objective, as well as to size the engines, maximum fuel loads, and structural weights, as described in Section II.C.

2. $V_{\mathrm{MC_G}}$-proxy: This is an off-design point which is used to size lateral control authority, as described below. This condition is analyzed on the ground at sea level at a specified speed.

3. Rotation: This is an off-design point which is used to size pitch control authority, as described below. This condition is analyzed on the ground at sea level at a specified speed greater than $V_{\mathrm{MC_G}}$.

*2. Design Variables*

The geometric design variables for each component of the geometry are described below. These are illustrated in Figure 7 and summarized in Table 2.

American Institute of Aeronautics and Astronautics

**Table 2: Geometric design variables. Blank entries imply no freedom, and the subscript 0 indicates the initial value.**

| Component | Span, $b$ | Quarter chord sweep, $\Lambda_{c/4}$ | Dihedral, $\Gamma$ | Root chord, $c_r$ | Taper, $\lambda$ | Twist, $\theta$ | Section, $t/c^{1,2}$ |
|---|---|---|---|---|---|---|---|
| Centerbody[3] | Cabin width $\leq b$ | | | $0 \leq c_r$ | $0 \leq \lambda$ | | $0.5(t/c)_0 \leq t/c$ |
| Transition | $0 \leq b$ | $\Lambda_{c/4}{}^4$ | | $0 \leq c_r$ | $0 \leq \lambda$ | $-10° \leq \theta \leq +10°$ | $0.8(t/c)_0 \leq t/c$ |
| Wing[5] | $0 \leq b$ | $30° \leq \Lambda_{c/4} \leq 55°$ | | $0 \leq c_r$ | $0 \leq \lambda$ | $-10° \leq \theta \leq +10°$ | $0.8(t/c)_0 \leq t/c$ |
| Winglet[6] | $0 \leq b$ | $30° \leq \Lambda_{c/4} \leq 55°$ | | $5\,\text{ft} \leq c_r$ | $0 \leq \lambda \leq 1$ | $-10° \leq \theta \leq +10°$ | $0.8(t/c)_0 \leq t/c$ |
| Fin[7] | $0 \leq b$ | $35° \leq \Lambda_{c/4} \leq 45°$ | $0° \leq \Gamma \leq 4°$ | $c_r = c_{r_0}$ | $0 \leq \lambda$ | | |

[1] The section design variables have significant freedom, and it is only the resulting $t/c$ which is limited. The $t/c$ bounds are presented here.

[2] The location of the section shape variables is indicated in Figure 7.

[3] The trailing edge sweep cannot be positive, i.e. the $x$-coordinate of the trailing edge at the outboard of the centerbody cannot be aft of the centerline trailing edge.

[4] Technically, transition sweep is free but has no bounds; rather the bounds are on wing root movement, which cannot be more than 8.5 ft.

[5] The wing tip chord is required to be greater than 3 ft. In the case of the winglet-equipped HWB, the winglet root chord bound overrides this, and enforces a wing tip chord no less than 5 ft. The increased wing tip chord for the winglet-equipped HWB is to account for winglet mounting accommodations.

[6] The aspect ratio of the winglets is constrained to be $\mathcal{R} \leq 4$.

[7] While the fin span and taper are free, the aspect ratio is constrained to be $1.4 \leq \mathcal{R} \leq 1.8$.

American Institute of Aeronautics and Astronautics

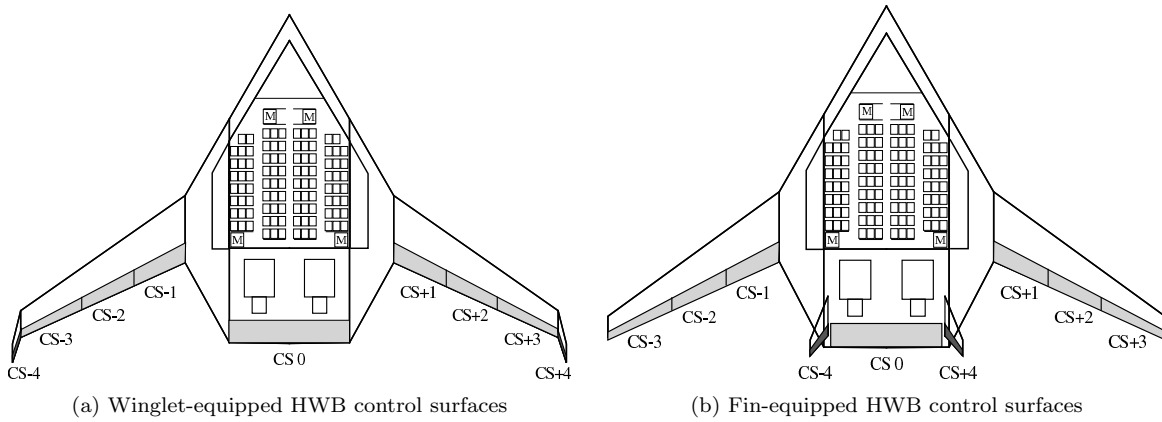(a) Winglet-equipped HWB control surfaces      (b) Fin-equipped HWB control surfaces

**Figure 8: Control surface layout and numbering.**

The primary planform variable for the centerbody is its length. The chord at the centerline and outboard edge (which corresponds with the edge of the cabin) are free to vary, but are constrained such that the hinge-line of the centerbody elevator is perpendicular to the symmetry plane. The section shape is free at the centerline and outboard station, and interpolated between. Twist is also variable at the outboard station. The span of the centerbody is free, but only to increase, which it never does.[a] The transition region connects the centerbody with the wing. The span, sweep, and taper of this region are free, as are the section and twist at the transition root and tip stations. The wing span, sweep, dihedral, taper, and twist are design variables, as are the section shapes at the wing root, tip, and two stations in between. The wing tip chord is constrained to be greater than 3 ft. For the winglet-equipped HWBs, the winglet span (height), sweep, and taper are design variables. The section shapes at the winglet root and tip are free, as is the twist (toe angle.) The winglet root chord must be greater than 5 ft to provide for wing mounting accommodations. The winglet aspect ratio is constrained to be no greater than 4. For the fin-equipped HWBs, the span and taper of the fin are design variables, with root chord, twist, and sections being fixed. The fin sweep and aspect ratio are free, but given limited freedom, $35° \leq \Lambda_{c/4} \leq 45°$ and $1.4 \leq A\!R \leq 1.8$, respectively. Since the fin weight model is based only on wetted area, the optimizer would increase sweep and span as much as possible while providing the required fin area for the S&C requirements. Thus, the quarter chord sweep and aspect ratio are constrained to be near values typically seen in the literature for HWB fins. There are a total of 197 and 149 free geometric parameters, for the winglet and fin-equipped HWBs, respectively. Note that the number of geometric design variables is higher, on the order of 1,000, but many of these are linked through linear constraints.

For all designs considered, there are nine control surfaces, numbered as shown in Figure 8. The chord of the elevator, CS 0, is 10% of the centerbody length, and its span covers the centerbody width (with

[a]For the narrow centerbody versions to be presented later, the centerbody span is allowed to decrease to match the width of the new cabin, in which case the quarter-chord sweep is fixed.

American Institute of Aeronautics and Astronautics

the exception of the fin-equipped designs, where it stops inboard of the fins). The wing mounted elevons, CS±1,2,3, have chords of 28% of the local chord, and are each 1/3 of the wing span. The winglet-mounted rudders, CS±4, are 30% of the local chord, and span 80% of the winglet height. The fin-mounted rudders are 30% of the local fin chords, and span 77% of the fin span. The elevator and elevons are only given freedom for pitch control, i.e. they cannot contribute to yaw control through differential drag. They are only utilized at the rotation point, with 1/3 of the maximum 25° travel permitted at this point. The rudders are only utilized at the $V_{\mathrm{MC_G}}$-proxy point, with their full 30° of travel. For the elevator and elevons, a positive deflection, $\delta$, is taken to be trailing edge down, while a positive rudder deflection moves the trailing edge to the left side of the aircraft (produces a negative $C_n$).

*3.  Constraints*

In addition to the constraints on geometric freedom presented in Table 2, some additional geometric constraints are enforced. The primary constraint which largely drives the shape of the centerbody is the cabin shape constraint. A polyhedron is constructed which encloses the passenger compartment, cockpit, and cargo holds. This surface, which is shown together with the optimized results below, forms a constraint such that the centerbody OML must reside outside of this polyhedron. The cargo hold, which is included in the polyhedron shape constraint, is housed in the transition region, as illustrated in Figure 5.

Sufficient volume is required in the wings for fuel storage. Usable wing volume is calculated by multiplying the wing OML volume by a factor to account for the volume of the wing box, assumed to be between 20-70% chord, together with a utilization factor to account for usable volume within the wing box. This results in $V_{\mathrm{wing,\ usable}} = 0.576 V_{\mathrm{wing,\ OML}}$. In addition, no fuel is stored within 5 ft of the wing tip/base of the winglet for lightning strike requirements. The usable wing volume, which does not include the winglet, must be greater than the required fuel volume. A tip strike constraint prevents excessive span and sweep which would severely limit attitude near the ground. This constraint ensures that with the MLG uncompressed and one wheel on the ground, a roll angle of 9.5° and pitch angle of 9.0° are possible. A minimum ground clearance constraint is also enforced, where the minimum distance between the underside of the aircraft and the ground is 3 ft with the MLG uncompressed.

The following S&C constraints are imposed.

1. Cruise: At the cruise point, trim and longitudinal static stability constraints are applied. That is, lift equals weight, the aircraft is trimmed in pitch, and the static margin, $K_n$, is constrained. It is assumed that unconventional aircraft such as the HWB will not enter service before the 2030s, and that within this timeframe, augmented stability controllers will be available which can demonstrate sufficient reliability such that certification of an aircraft with some degree of instability will be possible.
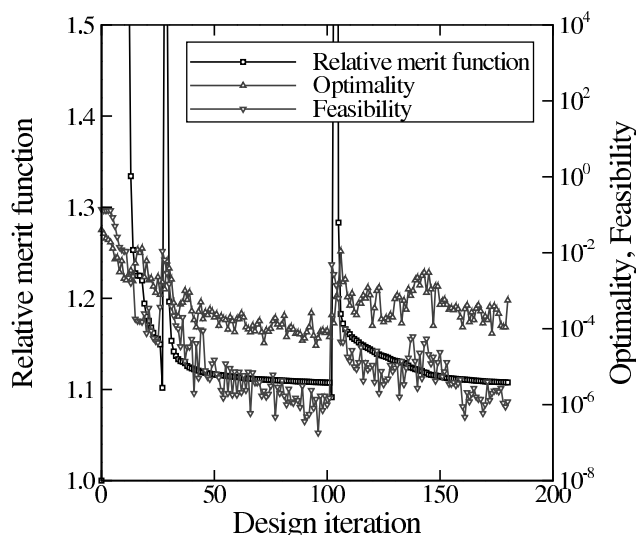
American Institute of Aeronautics and Astronautics

**Figure 9: Convergence history for the HWB100W optimization.**

It is thus required that the static margin with respect to the aft-most CG be no less than $-4\%$ MAC at cruise. The static margin is calculated via a finite difference with respect to the angle of attack, with $\Delta\alpha = 0.1°$.

2. $V_{\mathrm{MC_G}}$-proxy: This is a static proxy for a $V_{\mathrm{MC_G}}$ requirement to ensure sufficient lateral control authority with one inoperative engine (the left engine is assumed to be inoperative.) It is essentially the same as a minimum control speed in air ($V_{\mathrm{MC_A}}$) condition with zero bank angle. A required $V_{\mathrm{MC_G}}$-proxy speed is specified and lateral trim must be attainable at this speed on the ground (ground effect included.) This constraint is analyzed at low weight with the aft-most CG.

3. Rotation: A take-off rotation constraint ensures sufficient pitch control at a desired rotation speed, by ensuring a pitch acceleration of $3\,\mathrm{deg/sec^2}$ is attainable. Rotation occurs about the MLG contact point (CP) at full SLS thrust. This constraint is analyzed in ground effect and at both low and high weight conditions with different forward perturbations of the CG from the baseline loading curve.

# IV.  Optimization

The optimization procedure begins with a single-point optimization of the winglet-equipped design at the cruise point with the objective of minimizing drag subject to trim constraints, i.e. no static margin or off-design S&C constraints. Only the section and twist variables shown in Table 2 are active, i.e. the planform is fixed. This produces 1) a good starting point for the multipoint optimization, 2) a shock-free design on which to perform the grid convergence study to determine the best grid size and force correction factors, as described in Section II, and 3) provides the normalization factors for use in the multipoint
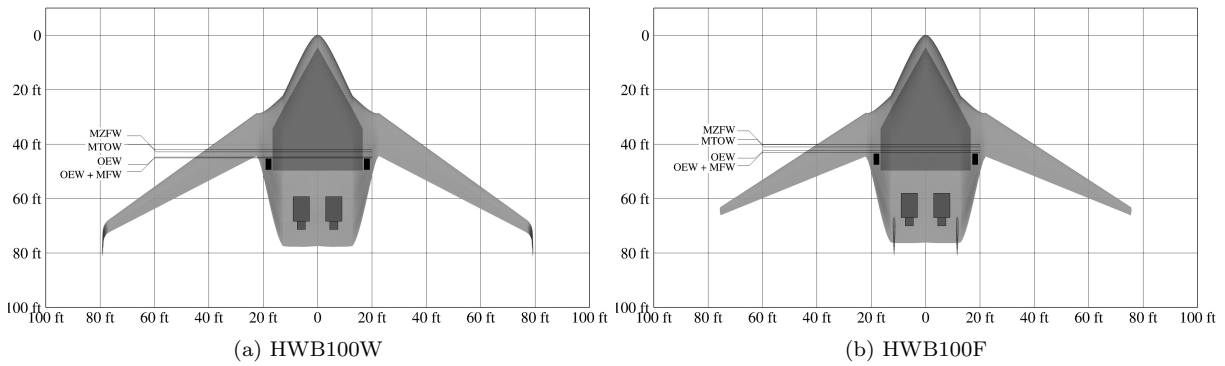
American Institute of Aeronautics and Astronautics

Note: 1) The overlaid polyhedron is the cabin shape requirement.
2) MLG and engines shown to illustrate MLG CP and engine/thrust location only.

**Figure 10: Optimized design planforms, with CG locations at different loading conditions indicated.**

optimization composite objective function. The fin-equipped HWB optimization begins from the optimized winglet-equipped design.

The multipoint S&C-constrained optimization convergence history for the winglet-equipped configuration is shown in Figure 9. The merit function is the objective (when constraints are satisfied), and optimality and feasibility are measures of the optimization convergence and constraint satisfaction, respectively. Constraints are considered satisfied when feasibility is less than $10^{-4}$. The spikes in the merit function at design iterations 25 and 100 are due to restarts of the optimization. At times, e.g. iterations 25 and 100, the optimization was restarted with new solver parameters to increase robustness, or with slight changes in the problem formulation, such as adjusting some constraint bounds based on insight gained during the optimization. The optimization formulation described in Section III is that at the end of the optimization. When changes were made, the optimization was restarted from previously converged results. Each optimization required approximately 100-200 function evaluations, with each function evaluation requiring analysis (flow solutions and gradient evaluations) at four operating points (one for the design point, two for the off-design S&C analysis points, and one for the static margin finite difference evaluation). All of these analyses are performed in parallel.

The optimized designs, referred to as HWB100W for the winglet-equipped configuration, and the HWB100F for the fin-equipped configuration, are shown in Figure 10, with performance summarized in Table 3.

Since the optimizer used is gradient-based, there is no guarantee that any of the optima found in this paper are the global optimum. This could be addressed in future work using a multistart procedure such as that proposed by Chernukhin and Zingg.[26]

At the converged solution, all of the trim and S&C constraints are active, as are the fuel volume and tip strike constraints. The dihedral has gone to its upper bound of 4° for the HWB100W, but stops at 3° for the HWB100F. Since there is little performance penalty (as far as the considerations included in

American Institute of Aeronautics and Astronautics

Table 3: Performance of the optimized designs.

|  | HWB100W | HWB100F |
|---|---|---|
| MTOW [lb] | 121,100 | 118,900 |
| MZFW [lb] | 94,900 | 93,300 |
| OEW [lb] | 72,400 | 70,800 |
|    Body [lb] | 27,600 | 27,200 |
|    Wing [lb] | 11,700 | 10,600 |
|    Winglets/Fins [lb] | 530 | 630 |
|    Propulsion [lb] | 8,400 | 8,400 |
|    Fixed [lb] | 24,000 | 24,000 |
| Max fuel weight [lb] | 26,200 | 25,700 |
| Max payload [lb] | 22,500 | 22,500 |
| Cruise thrust (per engine) [lb] | 3,400 | 3,400 |
| SLS thrust (per engine) [lb] | 15,400 | 15,100 |
| Reference MAC [ft] | 42.4 | 42.4 |
| Length [ft] | 77.4 | 76.1 |
| Span [ft] | 158.2 | 151.2 |
| Reference area [ft$^2$] | 3,560 | 3,380 |
| Cruise AoA [deg] | +0.0 | −0.2 |
| Cruise drag [lb/cnts] | 6,110/84.3 | 5,960/86.6 |
| Cruise $C_L$ [–] | 0.162 | 0.168 |
| Cruise $L/D$ [–] | 19.3 | 19.4 |
| Cruise $K_n$[1][% MAC] | +1.6 | +0.7 |

[1] $K_n$ with respect to the CG at the cruise point. The $K_n$ constraint is relative to the aft-most CG location, and goes to its bound.

the optimization are concerned) from increasing dihedral, this indicates that the tip-strike constraint is not driving for the fin-equipped configuration. This fact also offers insight into the driving force behind the optimal wing planform. For the fin-equipped HWB configuration, the wing span and sweep are determined so as to minimize drag and weight, and to satisfy the rotation constraint, while the wing of the winglet-equipped HWB is largely driven by the need to move the winglets aft to satisfy the $V_{\mathrm{MC_G}}$-proxy constraint. This is reflected in the reduced wing weight and improved performance of the HWB100F, as discussed below. The reduced span and sweep does have implications for the static margin constraint, and this configuration exhibits more aerodynamic tailoring, as discussed in Section VI.B, than the HWB100W.

For the HWB100W, the winglet root chord (wing tip chord) has gone to its lower bound of 5 ft, as has its sweep, 30°. The wing tip chord of the HWB100F goes to its lower bound of 3 ft, as does the fin tip chord. The fin quarter chord sweep angle goes to its upper bound (45°), as does the aspect ratio (1.80). The AoA on the ground for both configurations goes to its upper bound of 2°. For both configurations, the wing root has moved to its forward limit. The fuel volume constraint largely drives the wing thickness, with the

thickness constraints only active at a few chord locations at the wing tips.[b]

Examining the design parameters shown in Table 3, a few points warrant noting. First, the empty weight fraction is slightly high for such a regional-class aircraft. From the OEW breakdown, it is clear that a substantial portion of the OEW is from the centerbody, up to almost 39%. This is a larger fraction than is seen for the fuselage of conventional aircraft. The centerbody weight model is largely driven by the projected area of the centerbody, thus, the large portion of the centerbody aft of the passenger compartment is a large contributor to OEW while not housing any payload, and should be a target for reduction. The size of this portion of the centerbody is partly due to the rate at which the centerbody OML can close after the cabin while maintaining an aerodynamically feasible pressure recovery, and partly due to the need to have the elevator aft to satisfy the rotation constraint, as will be shown in Section VI.C. One method of reducing the weight penalty associated with this area is investigated in Section V. Second, from Table 3, it can be noted that the cruise lift-to-drag ratio for both configurations is not particularly high compared to current state-of-the-art tube-and-wing aircraft. While the purpose of this work is not to compare the performance of HWB and conventional aircraft, the lift-to-drag ratio bears noting.[c] The wing loading for both configurations is quite low at 34-35 lb/ft$^2$ at MTOW. This suggests that higher lift-to-drag ratios can be attained by cruising at higher altitudes. Similar designs studied in Reference 8 attained their maximum lift-to-drag ratio at cruise altitudes in excess of 40,000 ft. While field performance is not considered in this work, this low wing loading would be beneficial in that regard.

There is uncertainty in the winglet weight due to the lack of a winglet-specific model. Secondary wing weights are not accounted for in this model, nor are any benefits due to inertial relief. Future work should include the development and incorporation of a winglet-specific model.

As was shown by Reist and Zingg,[8] and will be confirmed in Section V, these classically shaped HWBs with their wide centerbodies are not the most efficient configuration for regional class aircraft. However, the winglet/fin-based control conclusions above may be applicable to larger aircraft where wide centerbody HWBs are more efficient. Examination of larger classes of aircraft using the framework developed here could confirm this.

## A.    Control Solution

The control deflections and their resulting moments are shown in Figure 11 for the HWB100W. The control solution and control increments for the HWB100F are similar, with the exception of rudder effectiveness, which will be discussed below; hence only the HWB100W solution is shown. For both the $V_{\mathrm{MC_G}}$-proxy and rotation conditions, the controls go to their bounds. From Figure 11(b), it is evident that the most

---

[b]Recall that the $t/c$ constraints are enforced at several $x/c$ locations along the chord, and are relative to the initial section.
[c]All sources of drag are accounted for with the exception of nacelle-centerbody interference drag.

American Institute of Aeronautics and Astronautics
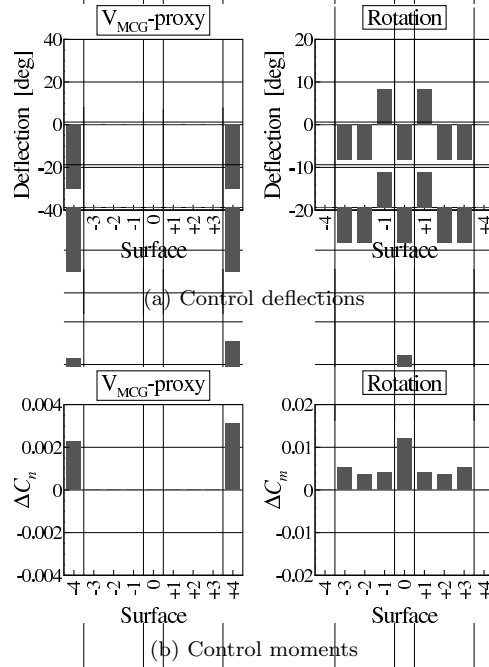
(a) Control deflections



(b) Control moments

Figure 11: Optimized HWB100W control deflections and effectiveness.

effective pitch control device is the centerbody elevator, followed by the outboard elevons. The inboard elevons produce a nose-up moment with positive deflection, as they act ahead of the MLG contact point. While low speed performance, e.g. $C_{L_{\max}}$, is not accounted for in the optimization, this positive deflection would be beneficial in this regard, as it would increase the local $c_l$, as opposed to decreasing it as happens on the outboard wing. The asymmetry in $\Delta C_n$ between the two rudders (CS±4) is due to the drag increment induced by the rudder deflections giving contributions to $C_n$ of differing sign, which induces a yawing moment due to the rudder location on the winglets. Thus, the rudder on the side to which yaw is desired is more effective. Both rudders produce similar side force increments. This asymmetry is not present to nearly the same extent on the HWB100F due to the smaller lateral offset.

## V.  Narrow Centerbody Configuration

Previous work by the present authors[8] suggests that for regional-class aircraft, HWBs which consist of a narrower, more elongated, centerbody and more distinct wings, referred to in that work as a lifting-fuselage configuration, offer better fuel efficiency than classically shaped HWBs. In addition, as shown above, the designs presented have excessive area aft of the cabin which contributes to a heavy centerbody. To investigate whether the findings in Reference 8 hold when S&C requirements are considered, and to determine if centerbody weight reduction is possible through an alternative cabin layout, narrow centerbody variants of the previously presented designs are investigated, which instead of the 12 abreast, 3-3-3-3, cabin
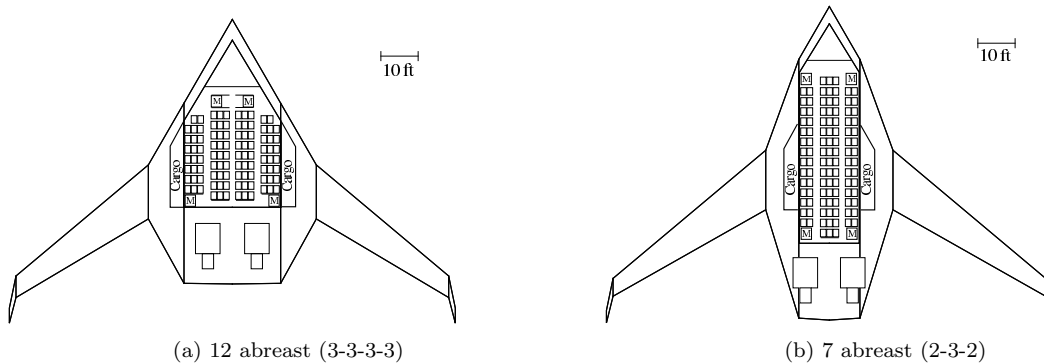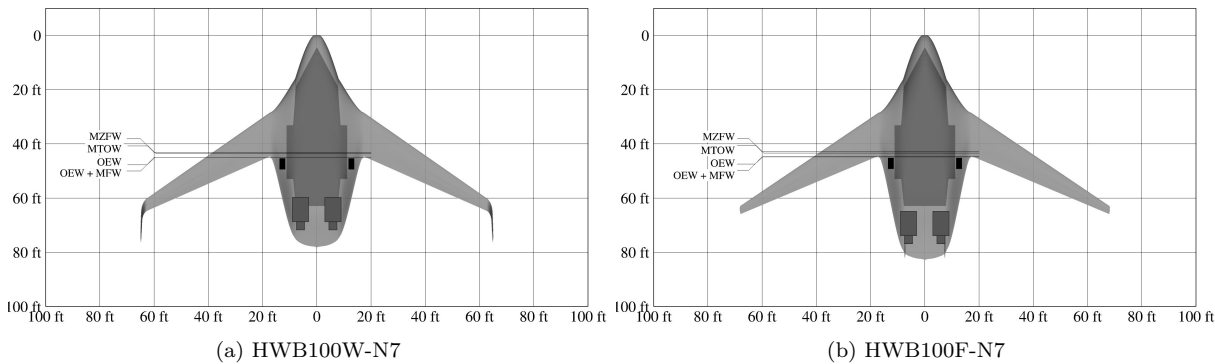
(a) 12 abreast (3-3-3-3)

(b) 7 abreast (2-3-2)

Figure 12: The original 12 abreast layout, and 7 abreast narrow centerbody variant.



(a) HWB100W-N7

(b) HWB100F-N7

Note: 1) The overlaid polyhedron is the cabin shape requirement.
2) MLG and engines shown to illustrate MLG CP and engine/thrust location only.

Figure 13: Optimized narrow centerbody designs, with CG locations at different loading conditions indicated.

layout, uses a 7 abreast, 2-3-2 layout. This layout is shown in Figure 12 alongside the original 12 abreast layout. This study is conducted for both the winglet and fin-based control configurations.

The optimization formulation is the same as that used for the previously presented cases, with new cabin shape polyhedra created to reflect the 7 abreast cabin shown in Figure 12(b). During the optimization, the span of the centerbody starts at the value of the HWB100W/F, and is free to decrease to the width of the narrower centerbody. Both winglet and fin-equipped versions of the 7 abreast are optimized. These optimizations are started from the previously converged cases presented in Section IV. The converged designs, referred to as the HWB100W-N7 and HWB100F-N7 for the winglet and fin-equipped configurations, respectively, are shown in Figure 13, with performance summarized in Table 4. All of the trim and S&C constraints are satisfied at the converged solution. The same geometric constraints are active as for the HWB100W/F cases.

The narrow centerbody designs have two primary advantages relative to the original HWB designs. First, the reduction of non-payload-carrying space aft of the cabin leads to significant centerbody weight savings of up to 6,000 lb, such that the centerbody contribution to OEW is reduced from 38% to 34%, and the overall OEW drops by up to 13%. Second, the cruise lift-to-drag ratio is up to 7% higher. This is a result of both

**Table 4: Performance comparison of all optimized designs, including the narrow centerbody designs.**

| | Winglet-equipped | | Fin-equipped | |
|---|---|---|---|---|
| | HWB100W | HWB100W-N7 | HWB100F | HWB100F-N7 |
| MTOW [lb] | 121,100 | 108,700 | 118,900 | 109,900 |
| MZFW [lb] | 94,900 | 85,800 | 93,300 | 87,100 |
| OEW [lb] | 72,400 | 63,300 | 70,800 | 64,600 |
|   Body [lb] | 27,600 | 21,600 | 27,200 | 22,200 |
|   Wing [lb] | 11,700 | 9,600 | 10,600 | 10,400 |
|   Winglets/Fins [lb] | 530 | 600 | 630 | 500 |
|   Propulsion [lb] | 8,400 | 7,500 | 8,400 | 7,400 |
|   Fixed [lb] | 24,000 | 24,000 | 24,000 | 24,000 |
| Max fuel weight [lb] | 26,200 | 22,900 | 25,700 | 23,000 |
| Max payload [lb] | 22,500 | 22,500 | 22,500 | 22,800 |
| Cruise thrust (per engine) [lb] | 3,400 | 2,900 | 3,400 | 2,900 |
| SLS thrust (per engine) [lb] | 15,400 | 13,200 | 15,100 | 13,100 |
| Reference MAC [ft] | 42.4 | 42.4 | 42.4 | 42.4 |
| Length [ft] | 77.4 | 78.1 | 76.1 | 82.8 |
| Span [ft] | 158.2 | 130.0 | 151.2 | 135.9 |
| Reference area [ft$^2$] | 3,560 | 2,800 | 3,380 | 2,880 |
| Cruise AoA [deg] | +0.0 | −1.5 | −0.2 | −0.9 |
| Cruise drag [lb/cnts] | 6,110/84.3 | 5,190/91.0 | 5,960/86.6 | 5,140/87.7 |
| Cruise $C_L$ [–] | 0.162 | 0.185 | 0.168 | 0.182 |
| Cruise $L/D$ [–] | 19.3 | 20.4 | 19.4 | 20.8 |
| Cruise $K_n$[1][% MAC] | +1.6 | −0.4 | +0.7 | −0.5 |

[1] $K_n$ with respect to the CG at the cruise point. The $K_n$ constraint is relative to the aft-most CG location, and goes to its bound.

reduced friction drag due to less wetted area and the higher wing loading of the narrow centerbody designs, which allows them to operate closer to the condition for their maximum lift-to-drag ratio at 36,000 ft. The wing loading, while higher than that of the HWB100W/F, is still quite low, and a lift-to-drag ratio benefit would be achieved by increasing the cruise altitude.

While the fin-equipped HWB has the potential to benefit the most from elongating the centerbody, as smaller fins can be used to satisfy the $V_{\mathrm{MC_G}}$-proxy condition, there is only minor aft movement of the fins. There is little increase in the centerbody length, with the optimizer instead opting to improve the cabin packing instead of elongating the centerbody, as shown in Figure 13. The centerbody length of the BWB100F-N7 does increase more than that of the HWB100W-N7 as expected, which allows for slight reduction in fin size due to their aft movement, but a small centerbody weight penalty is incurred. This leads to the HWB100F-N7 having a higher MTOW than the HWB100W-N7 - the opposite of the relationship between the winglet and fin-equipped configurations for the wide centerbody HWBs.

The interaction of the engines and fins poses a challenge for this configuration. As shown in Figure 13(b), the engines and fins are impractically close to each other. For this work, in order to maintain a fair comparison
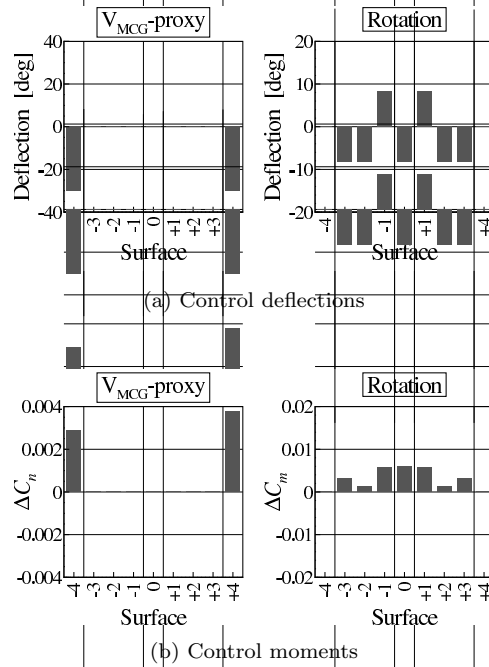
American Institute of Aeronautics and Astronautics

(a) Control deflections



(b) Control moments

**Figure 14: Optimized HWB100W-N7 control deflections and effectiveness.**

between the winglet and fin-equipped configurations, the engine position has not been changed to provide more clearance between the two. Should a narrow centerbody fin-equipped HWB be pursued, this conflict would have to be addressed, potentially by relocating the engines further inboard or in a centerline nacelle, for example.

## A. Control Solution

As with the 12 abreast designs, the longitudinal control behaviour between the winglet and fin-equipped narrow centerbody designs is similar, so only the HWB100W-N7 result is presented here. The most noticeable difference in the control effectiveness between the HWB100W and the HWB100W-N7, shown in Figure 14, is the reduction, of approximately 50%, in effectiveness of the centerbody elevator. This is primarily due to a 35% reduction in the elevator area. Comparing the HWB100W and HWB100W-N7 planforms, shown in Figures 13(a) and 10(a), respectively, it can be seen that there is a significant reduction in elevator span, but no increase in the centerbody chords. The required rotation authority is still maintained, however, as the aerodynamic nose-up moment required to meet the rotation constraint is less than for the wide centerbody designs, due, in large part, to the lower weight which acts ahead of the MLG CP and must be overcome in order to rotate.

# VI. Additional Considerations and Studies

The previous sections have demonstrated the ability of HWB aircraft to satisfy S&C requirements. Here, additional S&C considerations and sensitivities are examined. First, the ability of the previously optimized designs to satisfy additional S&C requirements is checked. Second, the sensitivity of the optimized shapes and performance to the previously studied S&C requirements is quantified. Finally, the effect of uncertainty in the CG location on performance is studied.

## A. Additional Control Requirements

Two S&C requirements which were not included in the optimization are: 1) the ability to trim at low speed at the extremes of the CG envelope, and 2) lateral control in a crosswind. Post-optimization checks for both of these requirements are conducted here for all of the previously optimized designs.

### 1. Low Speed Longitudinal Trim

To verify low speed trimmability, each of the optimized designs is analyzed for forward and aft CG locations – the conditions marked "MZFW" and "OEW+MFW" in the balance diagrams shown in Figure 15 – at sea level, Mach 0.2, and free air (no ground effect). Pitch trim is sought using the full range, 25°, of the elevator and elevons. Due to the negative static margin at low speed (as will be discussed below), to be conservative, zero thrust is used when trimming. Due to the number of control surfaces, the trim problem is underdetermined; thus, the solution which minimizes drag is sought. This is obtained by performing an optimization which minimizes drag subject to lift and pitch constraints, with the above mentioned control surfaces active, along with AoA. Due to their similar planforms, the winglet and fin-equipped configurations exhibit similar behaviour in low speed pitch control, so only the HWB100W and HWB100W-N7 are discussed here.

Trim is achievable for both designs. The aft CG case is the more challenging, but is trimmable without saturating the elevator/elevons. The BWB100W has more control power, such that it is trimmable with the centerbody elevator only. Due to the smaller centerbody elevator of the BWB100W-N7, it lacks sufficient control authority to trim the aircraft when used by itself, and the wing-mounted elevons are required.

An additional point to note is the movement of the neutral point at low speed. The neutral point location at Mach 0.20 (with control surfaces undeflected) is indicated in Figure 15. Between Mach 0.78 and Mach 0.20 the neutral point moves forward by 7.0% MAC and 10.8% for the BWB100W and BWB100W-N7, respectively. The larger forward movement for the BWB100W-N7 is due to more extreme aerodynamic tailoring as will be discussed below.

In addition to the movement caused by reducing the Mach number, deflection of the control surfaces

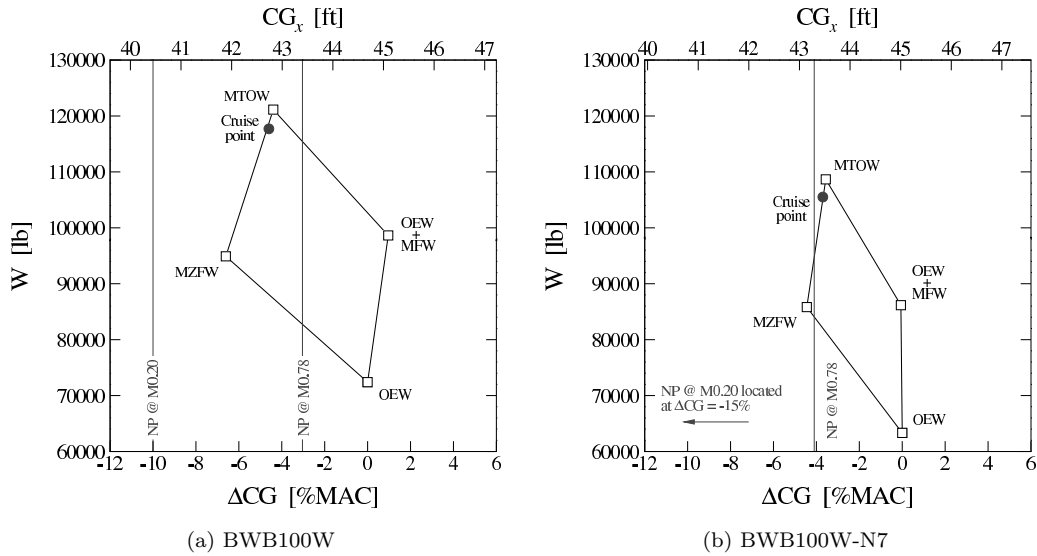American Institute of Aeronautics and Astronautics

**Figure 15: Balance diagrams for the BWB100W and BWB100W-N7. The neutral point locations at Mach 0.20 and Mach 0.78 are indicated by the vertical lines.**

moves the neutral point. The neutral point moves forward by up to an additional 5.4% and 7.6% for the BWB100W and BWB100W-N7, respectively. This results in highly unstable designs at this condition with $K_n = -16.5\%$ and $K_n = -22.7\%$ for the BWB100W and BWB100W-N7, respectively, when trimmed at the aft CG condition. This additional neutral point movement is due to nonlinearities resulting from large AoA and control deflections, and is thus most pronounced for the aft CG trim solution, which requires substantially larger control deflections than the forward CG solution. Such unstable aircraft are likely to be infeasible, and means of improving the stability characteristics at low speed must be addressed.

*2. Crosswind Lateral Control*

Due to the small lateral offset of the engines, it is possible that the crosswind landing condition would be critical for lateral control. To check this, a lateral trim solution is sought at a target landing speed with $11.5°$ of sideslip. Lateral trim is attained in all cases with less than $20°$ rudder deflection.

**B. Impact of Static Margin Requirement**

Longitudinal stability is potentially a challenge for HWB aircraft. For all of the designs presented, the static margin constraint goes to its bound. To investigate the effect of this constraint, in addition to the $K_{n_{\mathrm{aft}}} \geq -4\%$ requirement, two additional optimizations were conducted on the HWB100W and HWB100W-N7, one with a relaxed stability requirement of $K_{n_{\mathrm{aft}}} \geq -8\%$, and one with a more stringent requirement of $K_{n_{\mathrm{aft}}} \geq -1.5\%$. A comparison of the resulting optimized performance is given in Table 5. Performance for the designs with the $K_{n_{\mathrm{aft}}} \geq -4\%$ constraint can be found in Tables 3 and 4. As expected, aerodynamic

Table 5: Performance as a result of changing static margin requirement.

| | 12 abreast configuration | | 7 abreast configuration | |
|---|---|---|---|---|
| | $K_{n_\mathrm{aft}} \geq -8\%$ | $K_{n_\mathrm{aft}} \geq -1.5\%$ | $K_{n_\mathrm{aft}} \geq -8\%$ | $K_{n_\mathrm{aft}} \geq -1.5\%$ |
| MTOW [lb] | 120,100 | 121,700 | 108,000 | 109,300 |
| MZFW [lb] | 94,400 | 95,200 | 85,500 | 86,300 |
| OEW [lb] | 71,900 | 72,700 | 63,000 | 63,800 |
| Max fuel weight [lb] | 25,700 | 26,500 | 22,500 | 23,000 |
| Cruise drag [lb/cnts] | 5,930/81.6 | 6,220/85.4 | 5,070/88.9 | 5,220/90.6 |
| Cruise $C_L$ [–] | 0.161 | 0.162 | 0.184 | 0.184 |
| Cruise $L/D$ [–] | 19.7 | 19.0 | 20.7 | 20.4 |
| $K_n$ w.r.t. cruise CG [% MAC] | −2.4 | +4.3 | −4.5 | +2.2 |

performance degrades with an increasingly stable static margin requirement, with the wide centerbody HWB100W paying a larger penalty.

However, as will be discussed below, the design with the $K_n \geq -1.5\%$ requirement is highly point-optimized, and it would exhibit significantly degraded performance at off-design conditions.

While more restrictive static margin requirements would motivate increased sweep and/or aft movement of the wing, there is little change in the planforms between the designs optimized with the three different static margin requirements. This is for two reasons. 1) As discussed above, the rotation constraint favours placing the wing at its forward position, and the optimizer chooses not to move it aft with more restrictive static margin requirements. 2) The tip strike constraint prevents increasing wing sweep. This constraint is active in all cases. Thus, the optimizer has little freedom to move the neutral point aft as a more stable static margin is required. Instead, the optimizer uses local aerodynamic tailoring to move the local aerodynamic centers aft. This is illustrated in Figure 16 for the HWB100W, which compares the loci of the centers of pressure and aerodynamic centers for the designs optimized with the three static margin requirements. For the most unstable static margin requirement, the aerodynamic centers on the outboard wing are near the quarter chord, as expected.[d] As a more stable static margin is required, the aerodynamic centers move aft. This movement of the aerodynamic centers is achieved by tailoring of the pressure distributions, as evidenced in the pressure profiles shown in Figure 17 for the wing of the HWB100W. The pressure profiles for the case with $K_{n_\mathrm{aft}} \geq -8\%$ are well behaved, see Figure 17(a), but as the stability requirement is tightened, the optimizer adds the steep pressure recovery seen on the outboard sections in Figure 17(b). This pressure recovery is achieved isentropically, so the resulting drag increment is not drastic. This behaviour has been seen in past work by Reist and Zingg.[27] While the drag rise caused by this aerodynamic tailoring is not drastic, and the optimizer deems it more beneficial to add this feature instead of moving the neutral point aft by other means, it results in a highly point-optimized design, which incurs increased wave and form drag

---

[d]Strong 3D effects are present on the centerbody and transition region, leading to the deviation from the quarter chord for $2y/b \lesssim 0.4$.
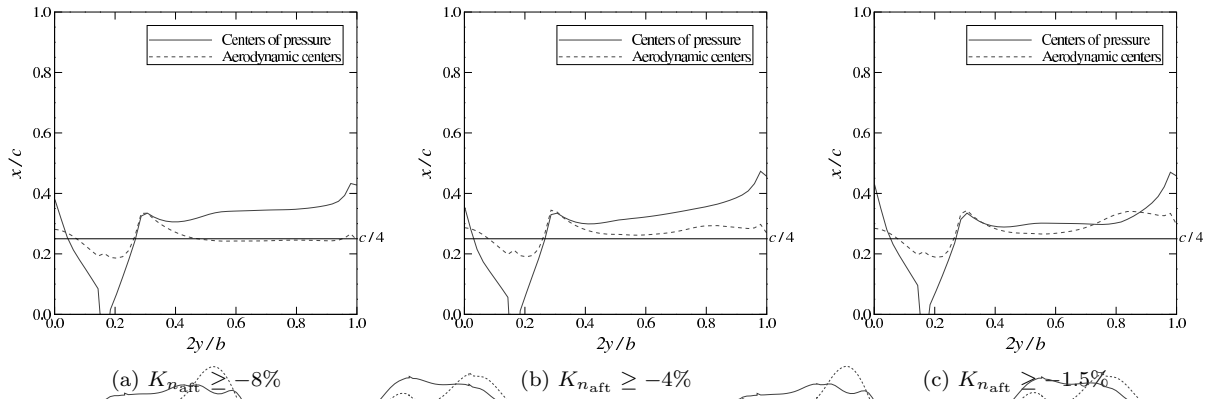
(a) $K_{n_{\mathrm{aft}}} \geq -8\%$    (b) $K_{n_{\mathrm{aft}}} \geq -4\%$    (c) $K_{n_{\mathrm{aft}}} \geq -1.5\%$

Figure 16: Impact of $K_n$ requirements on the spanwise distribution of the centers of pressure and aerodynamic centers for the HWB100W.



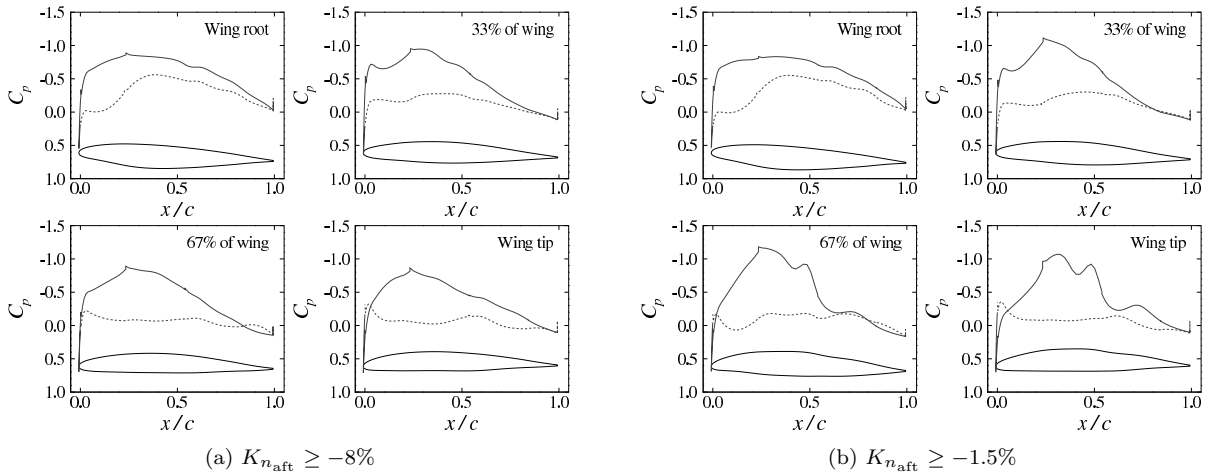(a) $K_{n_{\mathrm{aft}}} \geq -8\%$    (b) $K_{n_{\mathrm{aft}}} \geq -1.5\%$

Figure 17: Wing section shapes and pressure distributions on the HWB100W optimized with varying $K_n$ requirements.

at other flight conditions, as shown in Reist and Zingg.[27] The neutral point is moved aft only at the design point. Thus, the forward movement of the neutral point with change in speed is much greater than that of the HWB100W optimized for $K_{n_{\mathrm{aft}}} \geq -4\%$, such that at Mach 0.20 it ends up at the same position as the HWB100W optimized for $K_{n_{\mathrm{aft}}} \geq -4\%$. Similar behaviour is observed on the narrow centerbody variant, and is, in fact, more extreme than that seen on the HWB100W.

## C.    Impact of Rotation Requirement

To quantify the impact of the rotation requirement, the HWB100W and HWB100W-N7 are reoptimized, but without the rotation constraint. The resulting designs are shown in Figure 18, with performance information given in Table 6.

The absence of the rotation constraint allows for an 11% MTOW and a 6% lift-to-drag improvement for the HWB100W. For the HWB100W-N7, the improvement is 4% and 7% in MTOW and lift-to-drag
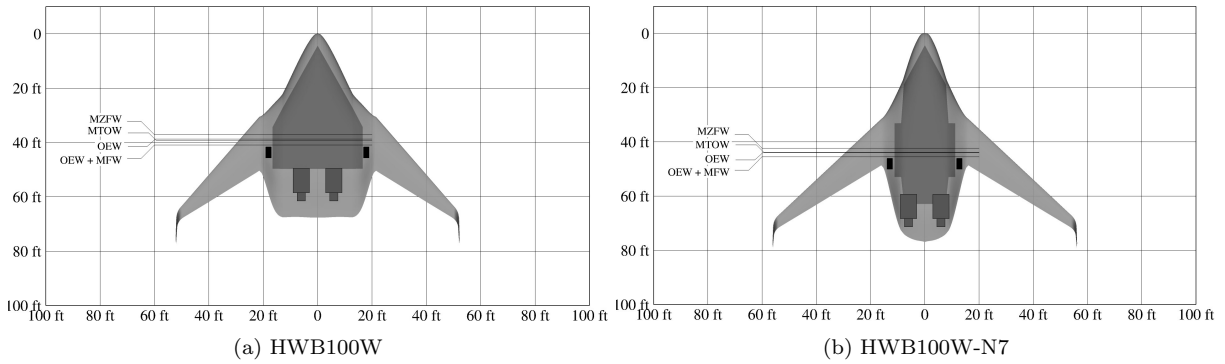
(a) HWB100W

(b) HWB100W-N7

Note: 1) The overlaid polyhedron is the cabin shape requirement.
2) MLG and engines shown to illustrate MLG CP and engine/thrust location only.

**Figure 18: Designs optimized without the rotation constraint.**

**Table 6: Performance of the HWB100W and BWB100W-N7 designs reoptimized with no rotation constraint.**

|  | HWB100W | HWB100W-N7 |
|---|---|---|
| MTOW [lb] | 107,200 | 104,300 |
| MZFW [lb] | 84,700 | 83,100 |
| OEW [lb] | 62,200 | 60,600 |
| Max fuel weight [lb] | 22,500 | 21,100 |
| Cruise drag [lb/cnts] | 5,090/89.5 | 4,640/89.6 |
| Cruise $C_L$ [–] | 0.183 | 0.195 |
| Cruise $L/D$ [–] | 20.4 | 21.8 |
| $K_n$ w.r.t. cruise CG [% MAC] | +1.4 | +0.3 |

ratio, respectively. The HWB100W sees a large reduction in centerbody length, and hence weight, as the aerodynamically optimal centerbody length is quite different than that required to satisfy the rotation requirement. For the HWB100W-N7, the aerodynamically optimal length and that required for the rotation constraint are less disparate due to the elongated cabin, and the centerbody weight reduction is thus less. The HWB100W-N7 optimized without the rotation constraint more closely resembles the HWB100W-N7 with the rotation constraint included than in the case of the HWB100W. This suggests that the narrow centerbody design is not driven as far away from the system optimal design by the rotation constraint, which is a further benefit of this configuration.

In addition, the spanwise lift distributions at cruise are shown in Figure 19 for the HWB100W and the version optimized without the rotation constraint. From these, the lack of lift carried on the centerbody when the rotation constraint is imposed is evident. This is due to the mechanism by which the centerbody obtains a strong nose-up moment which aids in the satisfaction of this constraint, although this limits the lift carrying ability of the centerbody. In contrast to this, a nearly elliptical lift distribution is maintained on the design which does not satisfy the rotation requirement. The same behaviour is seen on the narrow centerbody variants.

American Institute of Aeronautics and Astronautics

(a) HWB100W

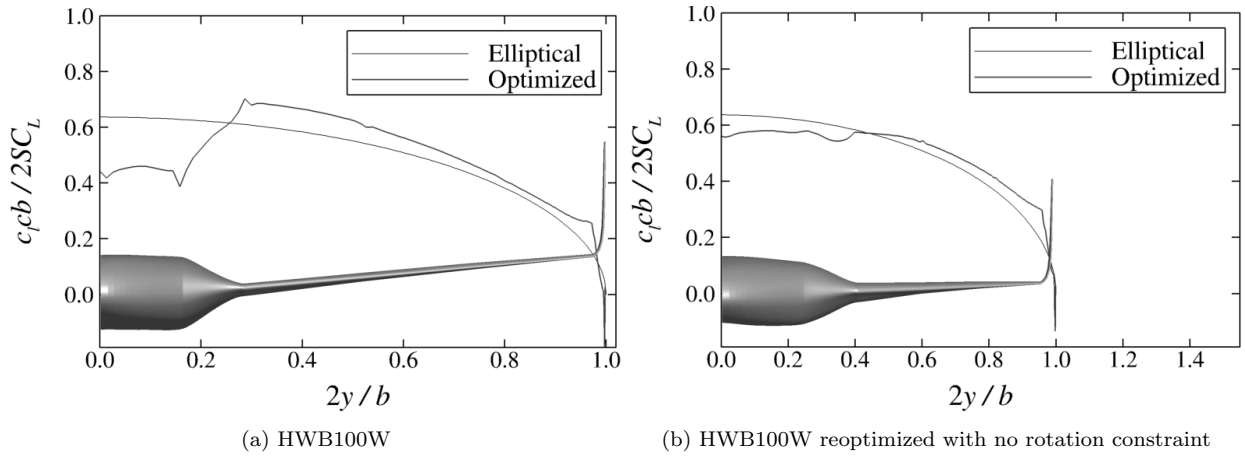(b) HWB100W reoptimized with no rotation constraint

Figure 19: Spanwise lift distributions at cruise on the HWB100W, and the HWB100W reoptimized without the rotation constraint.

While rotation must be achieved, having knowledge of the price paid to achieve it is beneficial. The significant performance improvements obtained when not subject to the rotation constraint suggest that alternative methods of achieving rotation authority, such as canards, telescoping landing gear, thrust vectoring, etc., may be worth studying as they could yield significant performance gains.

### D.  Impact of Center of Gravity Uncertainty

Since the S&C constraints depend strongly on the CG location and there is uncertainty in the CG estimates, a sensitivity study is performed with respect to CG location. To establish any potential trade-offs between the winglet and fin-equipped configurations, the BWB100W and BWB100F are reoptimized but with the CG perturbed by $\pm 10\%$ MAC from the computed location. To establish any trade-offs between the wide and narrow centerbody configurations, the BWB100W-N7 is also reoptimized with the same perturbation. The resulting impact on MTOW and cruise drag is shown in Figure 20.

The relative performance of the winglet and fin-equipped configurations is preserved if the CG is forward of the computed location by 10%, but changes if it is aft of the computed location by 10%. The relative performance, both in terms of weight and drag, does not change between the wide and narrow centerbody configurations due to a $\pm 10\%$ variation in the CG position.

## VII.   Conclusions

This work has developed a multi-fidelity MDO methodology which incorporates low-fidelity weight and balance models with Navier-Stokes predictions of aerodynamic performance and stability and control behaviour. This framework was used to compare the ability of both winglet and fin-equipped HWBs to satisfy S&C requirements, and to compare the resulting weight and cruise performance. It was found that both
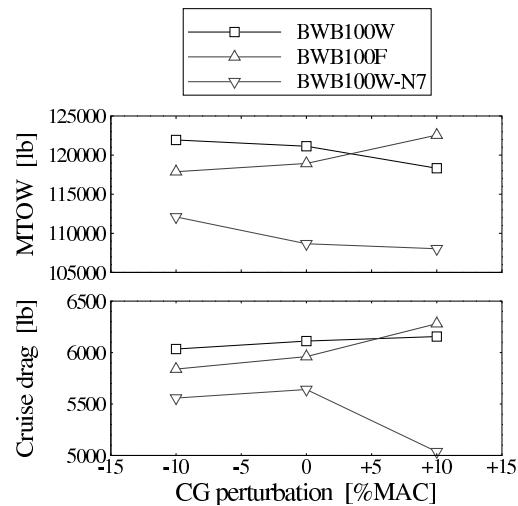
American Institute of Aeronautics and Astronautics

Figure 20: Impact of CG variation on MTOW and cruise drag.

winglet and fin-equipped configurations are capable of satisfying the S&C requirements studied in this work. The fin-equipped HWB was found to have an MTOW 2,200 lb (2%) lower than that of the winglet-equipped HWB, while also having a slightly higher cruise lift-to-drag ratio and 2.5% lower cruise drag. The reduced weight is due largely to a lighter wing, as the wing span and sweep are decoupled from the lateral control requirements and the wing can thus be made more efficient.

For both the winglet and fin-equipped configurations, a large portion of the OEW was due to the centerbody weight, which includes a significant amount of area aft of the cabin that does not house the payload. To reduce this, narrow centerbody variants of the original designs were investigated. These narrow centerbody designs give a significant reduction in weight, up to 10% in MTOW, and an increase in cruise efficiency, up to a 7% increase in the cruise lift-to-drag ratio, which yields up to a 15% cruise drag reduction. For the narrow centerbody variant, the relative performance of the winglet and fin-equipped configurations is reversed as compared to that of the wide centerbody designs, with the fin-equipped configuration being slightly heavier than the winglet-equipped configuration.

In addition to the S&C requirements included in the optimization, the ability to trim at low speed at the extremes of the CG envelope was also verified, as was the ability to land in a crosswind.

The impact of the degree of longitudinal instability was investigated for both the wide and narrow centerbody winglet-equipped HWBs by optimizing with static margin requirements between −8% and −1.5%. For the wide-body HWB, a MTOW and lift-to-drag ratio penalty is paid by requiring a −1.5% static margin instead of a −8% static margin. However, the method by which the neutral point was moved aft, through aerodynamic tailoring, is impractical due to its sensitivity to operating conditions. A similar penalty is paid for the narrow centerbody HWB. The rotation constraint was also found to be a large driver in the design, particularly for the wide centerbody configurations. While rotation must be achieved, this finding motivates

American Institute of Aeronautics and Astronautics

work to look at alternative means of obtaining rotation authority, such as thrust vectoring, canards, canted fins, etc., which may yield significant performance benefits.

All of the HWBs studied have MTOWs between 108,700 and 121,100 lb, which are greater than equivalent conventional designs, which are in the 100,000-115,000 lb range. It was also shown that the centerbody weight is a large contributor to the OEW, and should be a target for reduction. This work assumed the use of composites for the pressure vessel, but using structural technologies developed specifically for HWB aircraft, such as PRSEUS, should have the potential to reduce centerbody weight. In addition, for the narrow centerbody designs, an elliptical pressure vessel could be considered which may further reduce weight.

This work demonstrated the ability to control HWB aircraft and the efficiency of more elongated cabins for regional-class aircraft. Avenues for future work include the optimization of conventional aircraft using the same S&C-constrained optimization methodology in order to compare the performance of HWB and conventional aircraft. As mentioned above, alternative means of satisfying rotation requirements should be investigated. This study focused on regional-class aircraft, and studies to determine if the same winglet/fin-based control conclusions holds for larger aircraft are warranted. The use of higher fidelity models, particular structural models, would help build confidence in the results presented here, particularly with respect to the determination of centerbody and winglet weight and CG location.

## Acknowledgments

## References

[1] Vicroy, D. D., "Blended-Wing-Body Low-Speed Flight Dynamics: Summary of Ground Tests and Sample Results," *47th AIAA Aerospace Sciences Meeting and Exhibit*, AIAA-2009-0933, Orlando, FL, January 2009. doi:10.2514/6.2009-933.

[2] Rahman, N. U. and Whidborne, J. F., "A Lateral Directional Flight Control System for the MOB Blended Wing Body Planform," *International Conference on Control*, Manchester, UK, 2008.

[3] Rahman, N. U. and Whidborne, J. F., "Propulsion and Flight Controls Integration for a Blended-Wing-Body Transport Aircraft," *Journal of Aircraft*, Vol. 47, No. 3, 2010, pp. 895–903. doi:10.2514/1.46195.

[4] Cook, M. V. and de Castro, H. V., "The Longitudinal flying Qualities of a Blended-Wing-Body Civil Transport Aircraft," *The Aeronautical Journal*, Vol. 108, No. 1080, 2004, pp. 75–84. doi:10.1017/S0001924000005029.

[5] Garmendia, D. C., Chakraborty, I., and Mavris, D. N., "Method for Evaluating Electrically Actuated Hybrid Wing-Body

Control Surface Layouts," *Journal of Aircraft*, Vol. 52, No. 6, 2015, pp. 1780–1790. doi:10.2514/1.C033061.

[6]Garmendia, D. C., Chakraborty, I., and Mavris, D. N., "Multidisciplinary Approach to Assessing Actuation Power of a Hybrid Wing-Body," *Journal of Aircraft*, Vol. 53, No. 4, 2016, pp. 900–913. doi:10.2514/1.C033390.

[7]Mader, C. A. and Martins, J. R. R. A., "Stability-Constrained Aerodynamic Shape Optimization of Flying Wings," *Journal of Aircraft*, Vol. 50, No. 5, 2013, pp. 1431–1449. doi:10.2514/1.C031956.

[8]Reist, T. A. and Zingg, D. W., "High-Fidelity Aerodynamic Shape Optimization of a Lifting-Fuselage Concept for Regional Aircraft," *Journal of Aircraft*, Vol. 54, No. 3, 2017, pp. 1085–1097. doi:10.2514/1.C033798.

[9]Hicken, J. E. and Zingg, D. W., "A Parallel Newton-Krylov Solver for the Euler Equations Discretized Using Simultaneous Approximation Terms," *AIAA Journal*, Vol. 46, No. 11, 2008, pp. 2773–2786. doi:10.2514/1.34810.

[10]Osusky, M. and Zingg, D. W., "A Parallel Newton-Krylov-Schur Flow Solver for the Navier-Stokes Equations Discretized Using Summation-By-Parts Operators," *AIAA Journal*, Vol. 51, No. 12, 2013, pp. 2833–2851. doi:10.2514/1.J052487.

[11]Hicken, J. E. and Zingg, D. W., "Aerodynamic Optimization Algorithm with Integrated Geometry Parameterization and Mesh Movement," *AIAA Journal*, Vol. 48, No. 2, 2010, pp. 401–413. doi:10.2514/1.44033.

[12]Gill, P. E., Murray, W., and Saunders, M. A., "SNOPT: An SQP Algorithm for Large-Scale Constrained Optimization," *Society for Industrial Applied Mathematics Review*, Vol. 47, No. 1, 2005, pp. 99–131. doi:10.1137/S0036144504446096.

[13]Osusky, L., Buckley, H., Reist, T., and Zingg, D. W., "Drag Minimization Based on the Navier-Stokes Equations Using a Newton-Krylov Approach," *AIAA Journal*, Vol. 53, No. 6, 2015, pp. 1555–1577. doi:10.2514/1.J053457.

[14]Osusky, M., Boom, P. D., and Zingg, D. W., "Results from the Fifth AIAA Drag Prediction Workshop obtained with a parallel Newton-Krylov-Schur flow solver discretized using summation-by-parts operators," *31st AIAA Applied Aerodynamics Conference*, AIAA-2013-2511, San Diego, CA, June 2013. doi:10.2514/6.2013-2511.

[15]Gagnon, H. and Zingg, D. W., "Two-Level Free-Form and Axial Deformation for Exploratory Aerodynamic Shape Optimization," *AIAA Journal*, Vol. 53, No. 7, 2015, pp. 2015–2026. doi:10.2514/1.J053575.

[16]Zingg, D. W., Nemec, M., and Pulliam, T. H., "A Comparative Evaluation of Genetic and Gradient-Based Algorithms Applied to Aerodynamic Optimization," *European Journal of Computational Mechanics*, Vol. 17, No. 1, 2008, pp. 103–126. doi:10.3166/remn.17.103-126.

[17]Hicken, J. E. and Zingg, D. W., "A Simplified and Flexible Variant of GCROT for Solving Nonsymmetric Linear Systems," *SIAM Journal of Scientific Computing*, Vol. 32, No. 3, 2010, pp. 1672–1694. doi:10.1137/090754674.

[18]Abbot, I. H., von Doenhoff, A. E., and Stivers, L. S., "Summary of Airfoil Data," Tech. Rep. No. 824, NACA, Langley, VA, 1945.

[19]Mavriplis, D. J., Vassberg, J. C., Tinoco, E. N., Mani, M., Brodersen, O. P., Eisfeld, B., Wahls, R. A., Morrison, J. H., Zickuhr, T., Levy, D., and Murayama, M., "Grid Quality and Resolution Issues from the Drag Prediction Workshop Series," *Journal of Aircraft*, Vol. 46, No. 3, 2009, pp. 935–950. doi:10.2514/1.39201.

[20]Torenbeek, E., *Synthesis of Subsonic Airplane Design*, Delft University, 1976.

[21]Raymer, D. P., *Aircraft Design: A Conceptual Approach*, American Institute of Aeronautics and Astronautics, 5th ed., 2012. doi:10.2514/4.869112.

[22]Bradley, K. R., "A Sizing Methodology for the Conceptual Design of Blended-Wing-Body Transports," Tech. Rep. NASA/CR-2004-213016, NASA/Langley Research Center: Joint Institute for Advancement of Flight Sciences, 2004.

[23]Mukhopadhyay, V. and Sorokach, M. R., "Composite Structure Modeling and Analysis of Advanced Aircraft Fuselage Concepts," *AIAA Modeling and Simulation Technologies Conference*, AIAA-2015-3096, Dallas, TX, 2015. doi:10.2514/6.2015-3096.

[24]Roskam, J., *Airplane Design Part V: Component Weight Estimation*, Aviation and Engineering Corporation, 1989.

American Institute of Aeronautics and Astronautics

[25]Reist, T. A., *Scaling of Hybrid Wing-Body-Type Aircraft: Exploration Through High-Fidelity Aerodynamic Shape Optimization*, Ph.D. thesis, University of Toronto, 2016.

[26]Chernukhin, O. and Zingg, D. W., "Multimodality and Global Optimization in Aerodynamic Design," *AIAA Journal*, Vol. 51, No. 6, 2013, pp. 1342–1354. doi:10.2514/1.J051835.

[27]Reist, T. A. and Zingg, D. W., "Aerodynamic Shape Optimization of a Blended-Wing-Body Regional Transport for a Short Range Mission," *31st AIAA Applied Aerodynamics Conference*, AIAA-2013-2414, San Diego, CA, June 2013. doi:10.2514/6.2013-2414.